Journal of the European Ceramic Society 40 (2020) 4562–4571

Contents lists available at ScienceDirect

Journal of the European Ceramic Society

journal homepage: www.elsevier.com/locate/jeurceramsoc

Original Article

Influence of pores arrangement on stability of photonic structures during sintering

M. Dosta[a,*], K.P. Furlan[b], V. Skorych[a], S. Heinrich[a], R. Janssen[b]

[a] Institute of Solids Process Engineering and Particle Technology, Hamburg University of Technology, Germany
[b] Institute of Advanced Ceramics, Hamburg University of Technology, Germany

ARTICLE INFO

Keywords:
Discrete element method (DEM)
Sintering
Inverse opals
Ordered macroporous structures

ABSTRACT

Discrete Element Method (DEM) has been used for numerical investigation of sintering-induced structural deformations occurring in inverse opal photonic structures. The influence of the initial arrangement of template particles on the stability of highly porous inverse opal α-Al_2O_3 structures has been analyzed. The material transport, densification, as well as formation of defects and cracks have been compared for various case studies. Three different stages of defects formation have been distinguished starting with local defects ending with intrapore cracks. The results show that the packing of the template particles defined during the template self-assembly process play a crucial role in the later structural deformation upon thermal exposure. The simulation results are in very good agreement with experimental data obtained from SEM images and previous studies by ptychographic X-ray tomography.

1. Introduction

Photonic crystals and glasses are a class of materials with the capability of manipulating the electromagnetic radiation propagation and thereby, find application in solar thermophotovoltaic energy conversion devices and are also prospected as next-generation reflective thermal barrier coatings (rTBC) [1–3]. There are several types of photonic structures produced by a variety of processes. Direct photonic structures, usually comprised by polystyrene or silica monodisperse particles, are conveniently produced by a variety of self-assembly methods [4]. Meanwhile, inverse structures usually involve more complex processing and can be produced by co-assembly [5] and co-deposition [6,7], or via infiltration of templates by sol–gel [8], chemical vapor deposition (CVD) [9] or atomic layer deposition (ALD) [10]. ALD is especially interesting because of its capability for coating high-aspect ratio structures [11] and the possibility for the development of tailor-made atomically mixed systems. Ceramic-based inverse photonic structures have been produced using different techniques and various materials for the matrix such as silica [7], titania [10], alumina [12], mullite [13], zirconia [14] and yttria stabilized zirconia (YSZ) [7,15].

When these structures are exposed to high-temperatures (> 1000 °C), though, they undergo morphological changes that may hinder their final function, especially in the case of photonic applications. Among the structural changes are sintering shrinkage, pore enlargement, distortion, extensive grain growth and possible phase transformations. These changes are, as expected, directly dependent on the initial structural parameters and matrix composition [16]. In the latest years there has been a growing interest in the use of photonic glasses rather than photonic crystals, due to their capability of radiation reflection over a broad wavelength range instead of only of a narrow photonic band gap region. However, to our knowledge, studies about the structural changes in photonic glasses systems caused by high-temperature (> 1000 °C) exposure are scarce. We have been developing refractory inverse and hollow-sphere photonic glasses [13,15,17] for next-generation reflective thermal barrier coatings (rTBCs), which reduce the heat conduction by its highly porous structure whilst reflecting thermal radiation.

Several experimental techniques have been used to analyze the morphology of photonic structures. Scanning electron microscopy (SEM) is by far the most used technique, although followed by limitations such as charging, mechanical drift and only 2D qualitative information. Transmission electron microscopy (TEM) and focused ion beam (FIB) tomography are the ones with highest resolution, however with strong beam interaction and destruction, respectively. Synchrotron-based nano-tomography and ptychography have emerged as potential alternatives for 3D structural characterization of several porous materials [13,18–20], such as the ones studied in this work. In a recent work [13], we have shown that X-ray computed tomography

* Corresponding author.
E-mail address: dosta@tuhh.de (M. Dosta).

https://doi.org/10.1016/j.jeurceramsoc.2020.04.019
Received 29 January 2020; Received in revised form 7 April 2020; Accepted 10 April 2020
Available online 11 May 2020

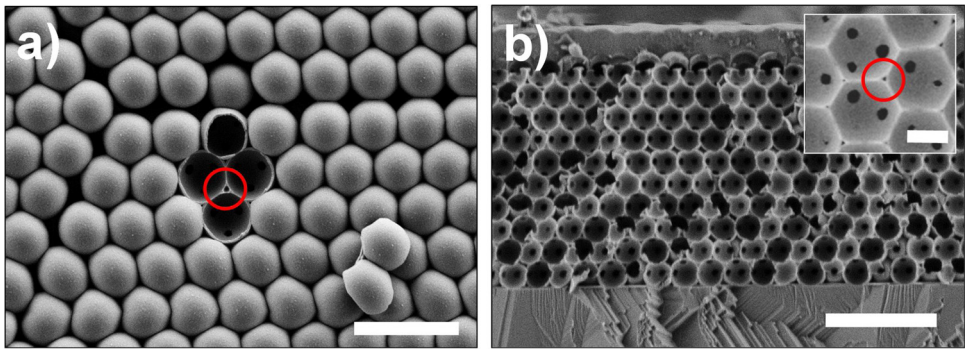

Fig. 1. Typical structures of inverse opal photonic crystals after ALD infiltration and template burn-out showing the hollow-shell structures (a) top view (b) cross section (inset) top-view of an ion-milled section. The red markers show typical interstitial sites for ALD-based photonic structures. Former PS template particles' size are 1.5 and 0.7 μm for (a) and (b), respectively. Scale bars are 3 microns and 500 nm at the inset. (For interpretation of the references to color in this figure legend, the reader is referred to the web version of this article.)

enables the quantification of 3D structural modifications at various scales caused by the high-temperature exposure. Nonetheless, the characterization of the high-temperature stability is mostly performed by post-mortem analysis and even though these analyses provide valuable information for the understanding of the structural destabilization with temperature and as input for simulation data, they don't allow for in-situ visualization of the structural destabilization pathways or for the identification of the sources of defect formation.

In this work, the discrete element method (DEM) approach, implemented in the simulation framework MUSEN [21], has been used to analyze the structural deformations occurring in inverse opals photonic structures exposed to high-temperatures. In general, the numerical modeling of material behavior during sintering can be performed on different time and length scales. Starting with molecular dynamic (MD) simulations on the nanoscale ending with semi-empirical densification models on the macroscale. One of the very promising simulation approaches which can be applied on the intermediate scale is the discrete element method (DEM). DEM is a meshless method, where the modeled material is represented as a set of interacting primary particles. This approach was initially developed for modeling the mechanical behavior of dry granular materials. However, in recent years it was also widely applied for the analysis of sintering processes. Material transport, densification or crack formation occurring in different types of structures have been analyzed using DEM [22–26]. The studies were carried out for free [24], pressure-assisted [27] and constrained sintering [23]. In most cases, DEM was applied for single-component systems, however, applications for composites consisting of two or more components can also be found [28,29]. Moreover, DEM simulation of sintering process was used to estimate the resulting material microstructure, later used to characterize mechanical characteristics of partially sintered samples [30]. Although this work focuses on the photonic materials application as next-generation reflective thermal barrier coating (rTBC), the structures exposed here have a high fraction of interconnected porosity, which makes them attractive for a variety of other technological applications, such as catalysts, solid oxide fuel cells and membranes [16,31,32].

1.1. Experimental synthesis and characterization of photonic crystals

Polystyrene (PS) particles with low coefficient of variation and an average diameter of 0.75 ± 0.02 μm and 0.76 ± 0.02 μm were used to produce templates for further infiltration via atomic layer deposition (ALD). Photonic crystals were produced via vertical convective self-assembly of 1.0 mg ml^{-1} PS-suspensions inside a humidity chamber (Memmert HCP 108) onto pre-cleaned single-crystal sapphire substrates (< 1-102 > orientation, Crystec GmbH) for 144 h at 70% RH and 55 °C. The cleaning process consisted of soaking and sonication in an alkaline detergent solution (Mucasol 1%, Brand, Merz Hygiene GmbH) for 1 h, brushing, rinsing with deionized water and drying with argon gas. Before immersion into the Teflon™ beakers, the substrates were further exposed to an oxygen plasma treatment for 20 min (Polaron PT7160, Quorum Technologies).

The PS templates were infiltrated by an ALD process with 300 cycles performed at 95 °C in a home-made reactor, using 30 sccm nitrogen as carrier gas. The precursors used were Trimethylaluminum, min. 98% (TMA, Strem chemicals) and deionized water (diH_2O), both kept at room temperature. Full-exposure mode was used and the pulse, exposure and pump time were 0.1/30/90 and 0.2/30/90 s for TMA and water, respectively. Film thickness and refractive index measurements were carried out by spectroscopic ellipsometry (SENProTM, SENTECH Instruments GmbH) onto silicon wafers (as received, < 100 > , native oxide layer, Si-Mat Silicon Materials) placed close to the templates during the ALD cycles. The growth per cycle (GPC) was in average 1.7 Å and the refractive index 1.65, consistent with our previous works [13,32,33]. After infiltration, the PS templates were removed by thermal burn-out at 500 °C (0.3 °C min^{-1}) in air atmosphere for 30 min, generating then the inverse opal photonic crystals. SEM images of typical generated structures can be visualized in Fig. 1. After burn-out of the PS template the photonic crystals are comprised by macro pores where the former PS spheres were located and thereby, a three-dimensional structure of interconnected macro pores is formed. Moreover, ALD-based photonic structures, such as the ones generated in this work, also present isolated nanopores located at the interstitial sites, due to the nature of the ALD process and the eventual blocking of these sites by the already-deposited films, which obstructs the precursors reach to these sites. One of these pores is highlighted by the red marker in Fig. 1a. The protective layer on top of the photonic crystal in Fig. 1b is only for imaging purposes and was not present during the heat treatments.

Photonic crystals were heat treated in a muffle furnace at 1200 °C for 1 h and 1400 °C for 4 h in air atmosphere. The heating rate was 5 °C min^{-1}. Scanning electron microscopy (SEM, Zeiss Supra 55 V P) was used to characterize the structures' morphology, both in surface and cross sections.

2. Modelling approach

2.1. Structure generation

The sintering behavior of inverse opal structures has been modeled with DEM. The porous rTBC layer of ceramics and the substrate were represented as a set of individual spherical primary particles. These particles were treated as individual objects and for each particle the Newtonian equation of motion has been calculated. To reduce the computational effort, periodic boundary conditions (PBC) in axial direction were applied. PBC were not defined in the vertical direction, which has allowed to investigate the rTBC interaction with the substrate.

To generate realistic initial structures, specifically to determine coordinates of all primary particles, a multi-staged approach has been developed. Here three main steps can be distinguished:

- Stage 1: Generation of the bulk phase
- Stage 2: Calculation of the pore positions
- Stage 3: Pores cutting and materials specification

Stage 1: Generation of the bulk phase

At first, a dense packing of primary particles that represent ceramics was generated. Generation was carried out using the previously developed iterative force-biased algorithm [21,34]. Initially, the particles are randomly placed into a cubic volume and overlaps between them are analyzed. Depending on the interparticle overlaps forces are calculated and particles are iteratively shifted to minimize the overlaps and to generate the packing. The algorithm is stopped when the maximal overlap in the system is smaller than the specified. This algorithm has been implemented into the simulation framework MUSEN and parallelized for graphics processing units (GPU). This allowed efficiently generate packings consisting of around six million primary particles.

Stage 2: Calculation of the pore positions

In the second stage, the coordinates of polymeric template particles were calculated. These coordinates directly determined the position of macro pores after the burn-out process. In the scope of this work, two types of template packings were analyzed. One group included the regular hexagonal close-packed (HCP) and face-centered cubic (FCC) structures. Here, the coordinates of pores were directly calculated depending on the specified lattice. For both FCC and HCP packings, four layers with 12 particles in each have been analyzed. The total number of polymeric particles (macro pores after burn-out) was equal to 48 and the diameter of each particle was equal to $D_{pore} = 0.762\,\mu m$. Thus, in the case of FCC and HCP structures the cuboid domain had a size of 2.29 μm x 2.64 μm x 2.63 μm (width x depth x height). These dimensions were calculated as $3D_{pore}$ x $D_{pore}\frac{4\sqrt{3}}{2}$ x $D_{pore}(1 + 3\frac{\sqrt{6}}{3})$.

The second group included stochastically generated random packings of polymeric particles with varied packing densities. On the one hand, such structures make it possible to analyze the influence of packing density. On the other hand, they can more realistically represent the defects occurring in self-assembled structures of polymeric template particles before burn-out, which are kept during the infiltration phase (in our case by ALD) and later reproduced in the inverse structures generated after burn-out [35]. Defects, such as vacancies, Frenkel defects, screw dislocations and cracks, are usual in self-assembled polymeric templates (colloidal spheres films) [12].

To generate random packings of polymeric template particles, a previously-described force-biased algorithm was used [21]. The particles with a diameter of 0.762 μm were generated into cubic domains with periodic boundary conditions over axial coordinates. The dimensions in axial coordinates were the same as in the case of the ordered packings, however, the height was slightly increased in 5% from 2.63 to 2.76. This was done to increase flexibility during packing generation and to allow particles to build stacking faults in vertical direction. In Fig. 2, two exemplary packings with different number of polymeric particles are shown. It is well known that an increase in packing density leads to ordering of structures [36]. This can be also observed in our results where increasing of packing density from 42 to 48 particles leads to their ordering. As result, the stochastically generated random close packed structures with high densities can be treated as ordered structures containing some stacking faults.

Stage 3: Pores cutting

Finally, the rTBC structure is created from previously generated bulk phase. Only those ceramic primary particles remain in the bulk, where for any pair of values $i \in [1. .N_{cer}]$ and $j \in [1. .N_{pol}]$ the following two conditions are satisfied:

$$\begin{cases} |C_{cer,i} - C_{pol,j}| \geq R_{pol} + R_{cer} \\ |C_{cer,i} - C_{pol,j}| \leq R_{pol} + L_{coat} - R_{cer} \end{cases} \quad (1)$$

where $C_{cer,i}$ and $C_{pol,j}$ are the coordinates of ceramic and polymeric particles, R_{cer} and R_{pol} are their radii, L_{coat} is the thickness of the ALD-coating layer, N_{pol} and N_{cer} are the number of polymeric particles and primary particles in bulk accordingly.

Complementary to the condition given in Eq. (1), several bottom layers of primary particles have been treated as a fixed substrate. Moreover, it was also considered that during ALD the substrate is also coated. In Fig. 3, a schematic illustration of all steps during the generation algorithm are shown.

2.2. DEM model

The DEM model proposed by Parhami and McMeeking [37] was used to simulate material densification. This model was developed for initial stage sintering without considering grain growth, and in recent years it has been effectively applied for different applications [23,24,28]. Between each two primary particles that are in contact, the forces in normal (F_n) and tangential (F_t) directions are calculated. The normal force consists of an attractive part, which causes material densification, and a dissipative part, which acts against relative motion:

$$F_n = \frac{\alpha}{\beta}\pi R\gamma_s - \frac{\pi a_s^4}{2\beta\Delta_b}u_{rel,n} \quad (2)$$

where parameters α and β depend on the ratio between grain-boundary and surface diffusion, R is the particle radius, γ_s is the surface energy, a_s is the contact radius between particles, Δ_b is the diffusion parameter and $u_{rel,n}$ is the relative velocity in normal direction of contact. The diffusion parameter is calculated depending on the diffusion coefficient D_{0b} as:

$$\Delta_b = \frac{\Omega}{kT}\delta_b D_{0b}\exp(-\frac{Q_b}{RT}) \quad (3)$$

where Ω is the atomic volume, k is the Boltzmann constant, T is the absolute temperature, δ_b is the grain boundary thickness and Q_b is the activation energy. The force in tangential direction consists only of

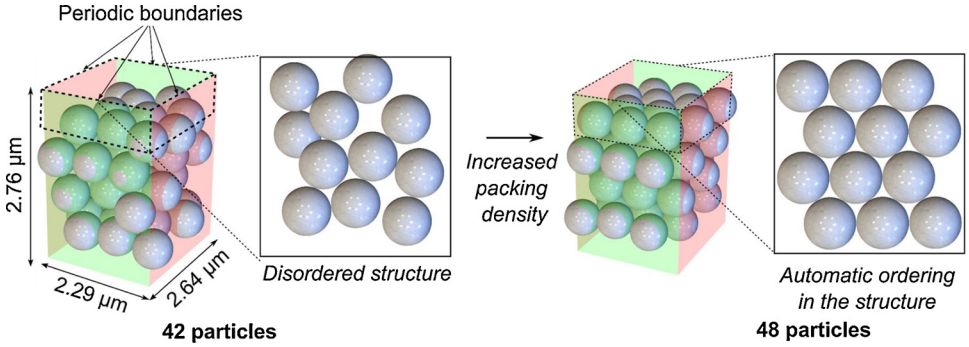

Fig. 2. Two exemplary packings of polymeric template particles with different packing densities. Three-dimensional view of the cubic generation domain and a top-view of the particles in the upper layer.

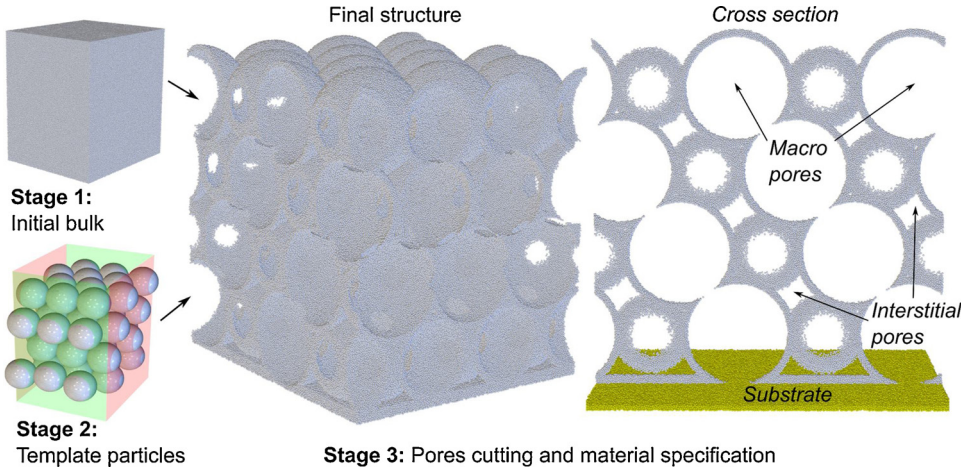

Fig. 3. Schematic illustration of the multi-staged structure generation algorithm to generate FCC packing. The cross-section on the right shows only a thin slice of Al_2O_3 and all particles of the substrate.

dissipative part, which acts against relative motion $u_{rel,t}$.

$$F_t = -\frac{\mu_{part}\pi a_s^2 R}{2\beta\Delta_b}u_{rel,t} \quad (4)$$

where μ_{part} is the dimensionless parameter to describe the viscosity. Yet, there is no consensus how to estimate this parameter, and discrepant values can be found in literature. More detailed information about the influence of this parameter on sintering behavior can be found in [23,25].

One of the main challenges related to the DEM application is the high computational effort due to the short simulation time steps. Since DEM is based on an explicit time integration scheme, the step size influences the numerical stability of the solution [38,39]. Especially in the case of the sintering process, where the size of primary particles is in the nanometer range, the calculation time is one of the limiting factors. As a mean to speed-up DEM simulation, mass scaling, where density of particles is increased in several orders of magnitude, can be applied [22,23,29,40]. Nevertheless, a posteriori analysis should always be done in order to check that such enlargement of particle inertia has no effect on the particle dynamics. For example, Heinrich et al. [22] have found that mass scaling to values $m_p < 8.6\cdot10^{-11}\frac{R^8}{\gamma_s\Delta_b}$ can be effectively used. In this study, a density scale factor of 10^{13} has been applied, which leads to a condition, in which $m_p < 4\cdot10^{-11}\frac{R^8}{\gamma_s\Delta_b}$.

For the DEM simulation the MUSEN framework has been used [21]. In recent years this framework has been successfully applied for different computationally expensive tasks [21,26]. The calculations in MUSEN are parallelized for graphics processing units (GPU) using CUDA platform. That allows to accomplish simulations consisting of several millions of particles in a reasonable time.

3. Results

3.1. Model parameters and generated structures

In the first stage of the generation algorithm, primary particles with a diameter of 15.2 nm have been generated into a cuboid volume with dimensions 2.29 μm x 2.64 μm x 2.76 μm for random and 2.29 μm x 2.64 μm x 2.63 μm for FCC and HCP packings. The initial porosity of the bulk phase was equal to ~35.8%.

In the second stage, different random packings of polymeric template particles with diameters of 0.762 μm have been generated and pores have been cut out. In the scope of this work, the influence of diameter deviations on the stability of rTBC was not investigated, and it was assumed that all pores have the same diameter. In Table 1, an overview of investigated packings is given. The packing porosity of polymeric particles and the number of ceramic primary particles, which remained in the structure after cutting out the macro pores, are listed here. The FCC or HCP packings reveal the highest macro pores fraction of 74%. Due to the increased generation domain, the random packings with same number of template particles (and thus macro pores, Case 5 in Table 1) have lower packing fraction of 71%. Both of them can be generally treated as photonic crystal structures. At the same time, packings with lower number of polymeric template particles, like in the Case 2, where packing porosity was equal to 37%, can be treated as photonic glasses.

Table 1
Packing information and the number of primary particles numbers in the investigated structures.

Case study	Number of polymeric template particles	Macro pores fraction [%]	Number of primary particles (in millions)
Random packings			
Case 1	38	58.89 ± 0.51	1.16 ± 0.022
Case 2	42	62.84 ± 0.68	1.211 ± 0.012
Case 3	45	66.27 ± 0.62	1.205 ± 0.019
Case 4	47	69.5 ± 0.35	1.207 ± 0.006
Case 5	48	71 ± 0.15	1.216 ± 0.007
Ordered packings			
FCC	48	74	1.099
HCP	48	74	1.098

With respect to the number of primary particles, it can be observed that an increase of template particles number from 38 to 48 leads to an increase in the coating material by volume of almost 5%. It should be also mentioned that ideally ordered FCC or HCP packings reveal a smaller amount of coating material compared to the randomly generated packings with the same number of pores. This is caused by the increased overall height of the analyzed volume in the structure from 2.63 μm to 2.76 μm.

The packing fraction of template particles influences not only the final structure of the rTBC, but also significantly affects the volume fraction of the deposited material. In experimental structures, the coating thickness will be the same for both photonic crystals and glasses, due to the individual surface reactions and self-limiting nature of the ALD process. However, since the surface area for the reaction is different, the volume fraction of the coating material will be different. To investigate this dependency, packings of polymeric particles in the range between 37 and 48 have been analyzed. In Fig. 4, two main characteristics are shown. The number of primary particles remaining in the structure after cutting out the macro pores is shown by the dashed red line. The packing fraction of template structure before ALD

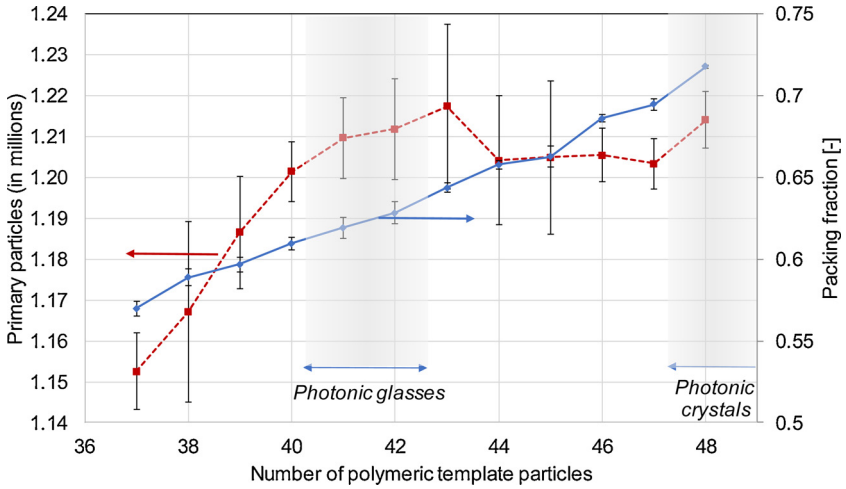

Fig. 4. Influence of number of polymeric particles generated into cubic volume on the packing fraction (blue solid line) and on the amount of coating material (red dashed line). (For interpretation of the references to color in this figure legend, the reader is referred to the web version of this article.)

and infiltration is illustrated by the solid blue line. This value is calculated without considering border effects occurring at the top of the packings.

The first dependency can be considered as the volume of the deposited material versus the total volume of the polymeric material. In the case of porous packings, where the number of template particles is less than 41, the amount of deposited material is almost linearly depending on the number of polymeric particles. The packings consisting of 41 particles reveal average packing density of ~61%. The increase of packing density from 41 to 48 particles has no significant influence on the volume of the deposited material. This is due to two main reasons: on the one hand, the total surface of the template material is increased. On the other hand, this effect is compensated due to the decreased interparticle distances.

An overview of the main parameters used for DEM simulation in all case studies is given in Table 2. In this study, the thermal gradient has been neglected and it was supposed that all particles have the same temperature.

The simulations have been performed using calculations on the hybrid CPU-GPU architecture. The operations related to the contact detection algorithm were executed on CPU and the calculation of forces, as well as the integration of motion, was carried out on GPU. Due to the use of such a parallelization strategy, the average calculation time for one case study on two different hardware configurations was equal to:

- 83 h: Intel Core i7-7700 K with NVIDIA GeForce GTX 1080 Ti;
- 36 h: Intel Xeon Gold 5118 with NVIDIA Quadro GV100.

Table 2
Main simulation parameters used in all case studies.

Parameter	Symbol	Value	Units	Reference
Simulation time step		10^{-8}	s	
Viscosity parameter	μ_{part}	0.05	–	[23,25]
Radius of primary particle	R	7.6	nm	
Pore radius	R_{pol}	381	nm	[13,33]
Surface energy alumina	γ_s	1.1	J/m^2	[23,24,41]
Surface energy substrate	γ_s	0.638	J/m^2	[42]
Grain-boundary thickness times diffusion coefficient	$\delta_b D_{0b}$	1.3×10^{-8}	m^3/s	[23,41]
Activation energy	Q_b	475×10^3	J/mol	[23,43]
Temperature	T	1473	K	[33]
Atomic volume	Ω	8.47×10^{-30}	< p	

3.2. Structural deformation

Due to the material sintering upon high-temperature exposure, significant structural deformations of the initial rTBC can be observed, as demonstrated for HCP pores packing in Fig. 5. To qualitatively characterize the structural deformation and to compare different case studies (different packings) we distinguish three main types of structural changes:

- Material transport at the top of the rTBC, pores deflection and overall vertical shrinkage
- Enlargement of interpore openings. Interpore openings are the former connection points between the template particles
- Formation of small defects, rupture of struts, interpore and intrapore cracks

Since the DEM model of sintering process (Eqs. (2)–(4)) does not consider grain growth, structural deformations which can occurring at further stages are not considered in this work.

3.2.1. Vertical and axial material transport

In Fig. 6, the top view for two different case studies, corresponding to a 'perfect' photonic crystal (FCC-packing) (Fig. 6a) and a photonic crystal with defects (Fig. 6b) are shown. Here, the primary particles are colored according to their velocity in *y*-direction during the simulation of temperature exposure. It should be noted, that, since in the DEM simulations the scaled time is used, the magnitude of the velocity given in the color bar does not directly represent real material velocity, but can be used to quantitatively analyze the material transport within the shells of the photonic structures (ALD coating). As it can be observed, the material transport takes place from sides to the top of each pore, which is mainly due to the flattening of the pore's curvature. In the 'perfect' photonic crystal case a symmetrical material transport on the surface of all shells can be observed, as a result of the periodic boundary conditions and axial symmetry of the structure. Conversely, in the case of non-ideal structures, even in densely packed states like in Case 3 (description in Table 1), the material has a higher degree of freedom for motion in axial or vertical directions and, as a consequence, the formation of heterogeneous zones can be observed, as depicted in Fig. 6b. The grade of the heterogeneity is strongly dependent on the porosity of the template packing. Such material transport can be a source of possible defects and cracks.

Moreover, during the sintering process, an enlargement of interpore connections can also be observed. These results are in good agreement with experimental results of Furlan et al. [33] for Al_2O_3:SiO_2 ALD-based

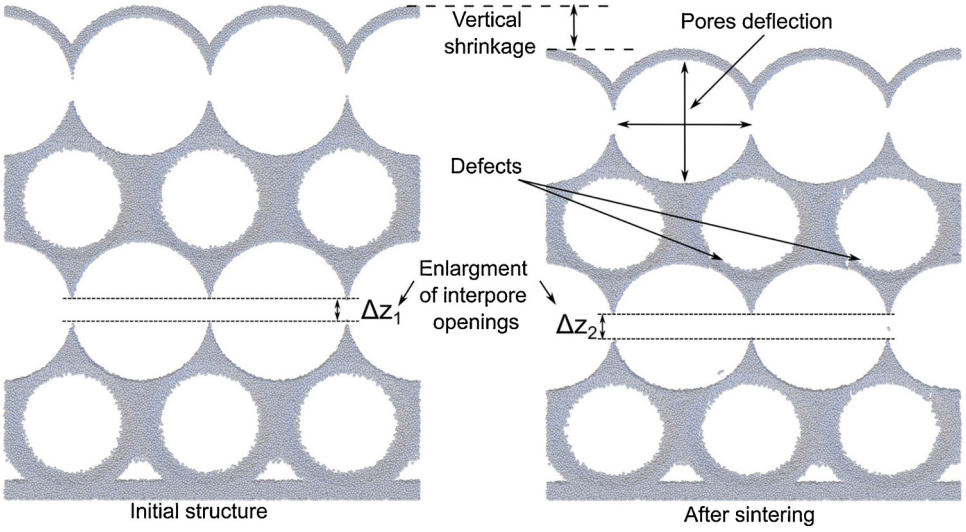

Fig. 5. Cross-section view of an Al_2O_3 photonic crystal structure with HCP packing before (left) and after thermal exposure (right).

inverse opal photonic crystals with a template size of 762 nm and by Sokolov et al. [8] for sol-gel based Al_2O_3 inverse opal structures.

As it is expected, the vertical shrinkage of rTBC strongly depends on the initial pore packings. In Fig. 7, the average vertical shrinkage for different case studies and for two different time points ($t_2 > t_1$) is shown. Analysis of vertical shrinkage for the final time point t_2 shows that ideally ordered FCC and HCP structures with template particles packing densities of 74% result in the smallest vertical densification of about 8.2%. The slight disordering in the system and decrease of the packing density to 71% and 69.5% for the case studies 5 and 4, respectively, leads to the slightly larger vertical deformation around 8.38%. This agrees with earlier experimental observations by ptychographic x-ray computed tomography [13], in which the 3D shrinkage in the overall photonic crystal structure accounted for 8%, including the vertical shrinkage measured by the difference between the periodicity of macropores prior (531 nm) and after (488 nm) sintering at 1400 °C for 4 h. However, the further decrease of the packing density to 66.3% and 62.8% for case studies 3 and 2 result in much larger deformations of 9.36% and 9.72%. Comparison of the vertical deformation for two different time points shows that for both sintering stages the deformation grade depends on the packing density almost linearly. Moreover, one can clearly observe that for t_1 the slope of the linear fit is less steep than for t_2, which can be directly linked to the sintering process and a more pronounced shrinkage for larger sintering times. Such results fit nicely to our earlier experimental observations of alumina inverse opal photonic crystals [33], for which an increase from 1 h to 4 h of dwell time at 1300 °C caused substantial changes in the structure morphology analyzed via SEM.

In summary, our results point out that in rTBCs with low packing densities, i.e. photonic crystals with defects and photonic glasses, the material has a larger degree of freedom for the motion in the axial direction (Fig. 6b), which also results in a larger vertical deformation. This could mean that although photonic glasses are better suited for reflective thermal barrier coatings in terms of reflectance capability, they suffer from larger vertical deformation, which could reduce its thermal stability if this deformation is linked to defect formation (analyzed in the next section).

3.2.2. *Formation of defects*

We distinguish three main categories of structural defects taking

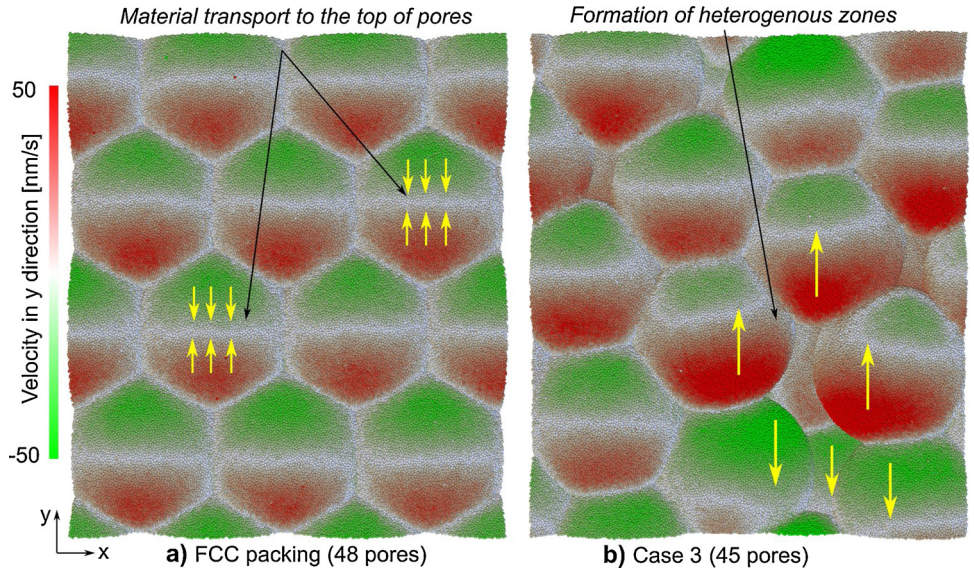

Fig. 6. Axial material transport for two different initial pore structures (top view). Symmetric material transport for FCC structure and formation of heterogeneous zones for Case 3.

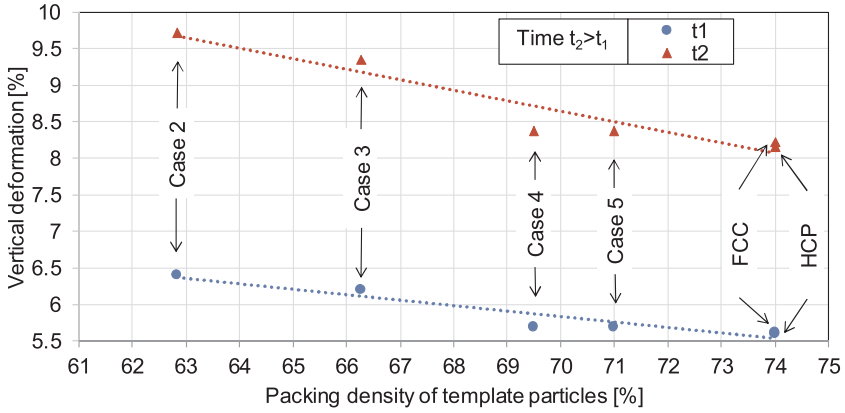

Fig. 7. Average vertical shrinkage for different case studies and for two different time points, where $t_2 > t_1$.

place in the photonic structures during initial stage sintering, namely:

- **Local defects**: defects smaller than 20 nm. Depending on their position and local stress distribution around these defects, they can be a source for crack initiation.
- **Interpore cracks**: small cracks with a typical length in the range 50–700 nm which occur on the surface of individual pores or at boundaries between adjacent pores. The rupture of struts is also considered as interpore cracks.
- **Intrapore cracks**: large cracks with lengths exceeding 700 nm and that are going through two or more pores. The identification of such cracks in highly-porous photonic structures is not trivial. A set of interpore cracks, such as ruptured struts, which are located on the same two-dimensional plane, are considered as one intrapore cracks.

The simulation results have shown that all the defects listed above occur almost in direct sequence, starting with the local defects followed by interpore and ending with intrapore cracks. Since the resolution of the DEM simulations performed is of the order of 15 nm, in this work we do not perform a detailed investigation of local defects, but rather of the interpore and intrapore cracks. Moreover, due to the limited height of the simulated rTBC structure, corresponding to 4 layers only, the analysis of delamination effects is not considered in this contribution.

Independently on the type of investigated structure, almost all cracks are initiated from the spherical interpore openings (former connection points between the template particles) and propagate to the center of adjacent opening which is formed by the contact with another macropore. On the left side of Fig. 8, the typical initial cracks that appear at the interpore openings are shown. With the solely purpose of improving visual representation, additional cylindrical bonds have been generated between the contacted particles. These bonds are only used during post-processing and do not have any influence on simulation results.

In Figs. 9 and 10, the formation of intrapore cracks in ideally ordered structures is illustrated. Here, as in Fig. 8, bonds were generated between contacted particles during post-processing. To aid the visualization of the deformations inside the structure, a top layer of around 300 nm was removed when generating the image after simulation. The formation of the intrapore cracks is initiated inside the structure and only on the later stages they are propagated to the outer rTBC surface. Due to the modeling of only initial stage sintering and the relatively small thickness of modeled rTBC, almost no cracks have been observed on the rTBC surface.

The particles and bonds in Fig. 9 are colored according to their velocity. Here, cracks which are going through more than one pore in vertical and horizontal direction are identified. In the case of ideally ordered structures, the defects often form two-dimensional planar surfaces. On the right side of Fig. 9 two main intrapore crack paths projected onto the surface of rTBC are shown and compared to the cracks observed from SEM images. Obtained numerical and experimental results are in very good agreement. Similar patterns are identified, where the intrapore cracks are propagating through centers of several macro pores.

For the quantitative characterization of defects, the relative positions of primary particles are analyzed. If any two primary particles were initially in the contact and if in the final state the distance between their surfaces is larger than a specific threshold, then these particles are marked to be part of a defect. The marked particles may belong to the same or to different defects. For all case studies, a distance of 12.16 nm (80% of particle diameter) was selected as the optimal threshold value. The value was chosen considering the following factors. On the one hand, too small threshold value leads to the appearing of noise, due to which some material deformations can be identified as cracks. On the other hand, too large values do not allow to detect cracks at all.

To analyze the size of the defects, the grouping of particles into the independent sets has been performed. If any two particles are identified to be part of the defect, and they are in contact, then it is assumed that both of them belong to the same defect. Thereby, the number of primary particles in the defect is directly proportional to the formation of the new surface.

In Fig. 11, the quantitative comparison of the defects for different case studies is shown. In Fig. 11a, the dependency of defects number from the number of primary particles per defect is shown. On the right side the average gap distances are illustrated. The average gap distance is calculated as:

$$\bar{x}_{gap} = \frac{1}{N_g}\sum_{i=1}^{N_g}\left(|C_{1,i} - C_{2,i}| - R_{1,i} - R_{2,i}\right) \quad (5)$$

where N_g is the total number of pairs of particles which are marked to be part of the defect, $C_{1,i}$ and $C_{2,i}$ are the coordinates of particle centers after sintering, $R_{1,i}$ and $R_{2,i}$ are the radii of particles.

From Fig. 11 it can be seen, that higher packing densities of template particles, i.e. 'perfect photonic crystals', lead to the formation of larger number of defects. For example, the number of defects considering the same defect-size range for 'perfect' HCP structures is about 130, whilst for the structures with packing densities ~71% (for case studies 4 and 5) this value is reduced to 97. However, comparison of the gap distances (Eq. (5)) for different case studies (Fig. 11b) shows that the average gaps are smaller for HCP structures. The structures with much lower packing densities like Case 2 with density of 64% reveal much smaller number of defects as well as smaller gaps.

Such behavior is a result of the relaxation of sintering-induced stresses. In the case of photonic glasses-like structures, like in Case 2 or 3, the coating material has a high degree of freedom for the motion in the axial direction (see Fig. 6). As a result, the stresses are relaxed

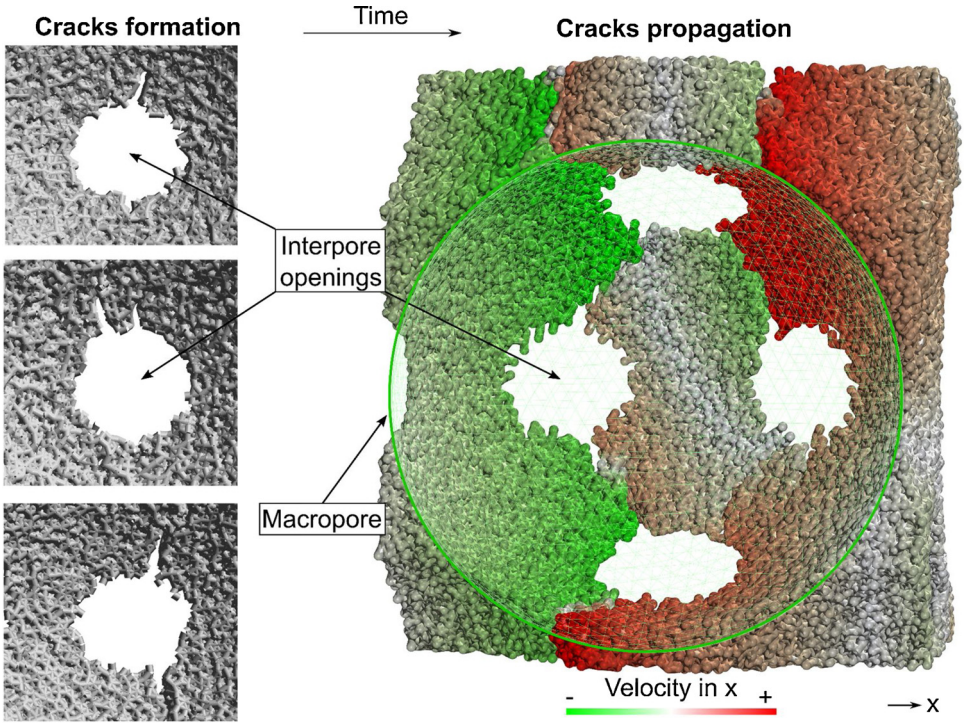

Fig. 8. Typical formation of cracks at interpore openings illustrated for the FCC packing. Initial formation for three different openings (left) and further stages of crack propagation for a single pore (right).

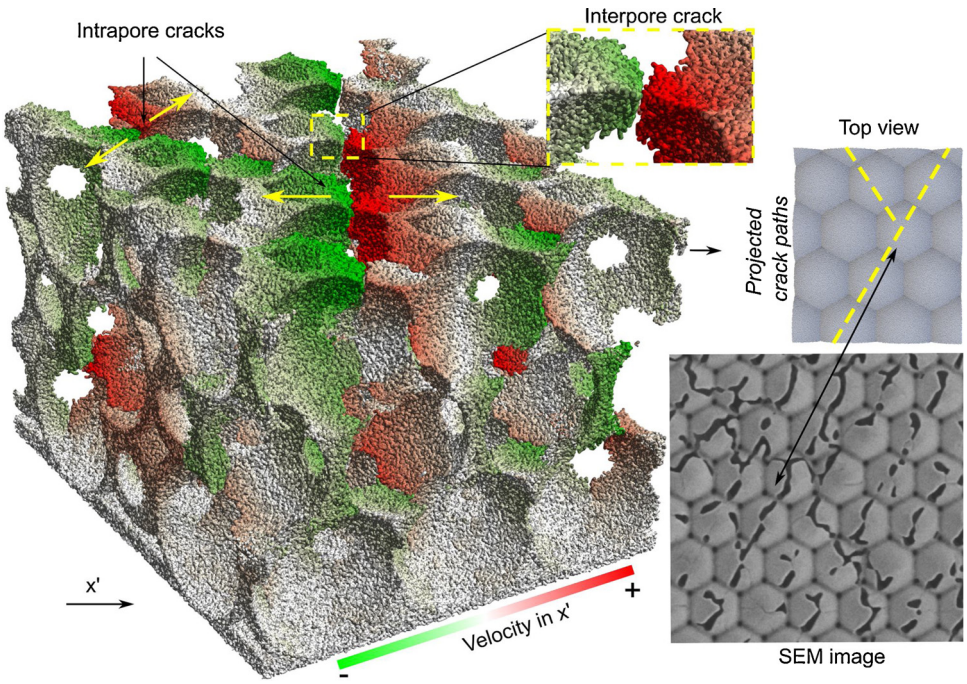

Fig. 9. Typical intrapore cracks occurring in HCP structure (left). Crack paths projected to the rTBC surface and their comparison to experimental results (right).

through the overall larger deformation of structure (Fig. 7). Contrary to this, highly-packed beds (photonic crystals) have less capability for stresses relaxation, which lead to the formation of a higher number of inter- or intrapore defects inside rTBC. Furthermore, significant differences between ideally ordered structures (FCC and HCP) and close-packed beds containing initial defects (Case 4 and 5) can be observed. For these structures, a higher number of defects are observed in comparison to photonic glass-like structures. However, in rTBCs for cases 4 and 5, larger gaps are formed compared to FCC or HCP due to the non-homogenous distribution of sintering stresses. As a result, the stress relaxation is enhanced in these structures compared to FCC or HCP packings, that generally leads to the formation of fewer defects.

4. Conclusions

Sintering-induced deformations of inverse opal structures have been numerically investigated using discrete element method. For this purpose, a multi-staged structure generation algorithm has been proposed

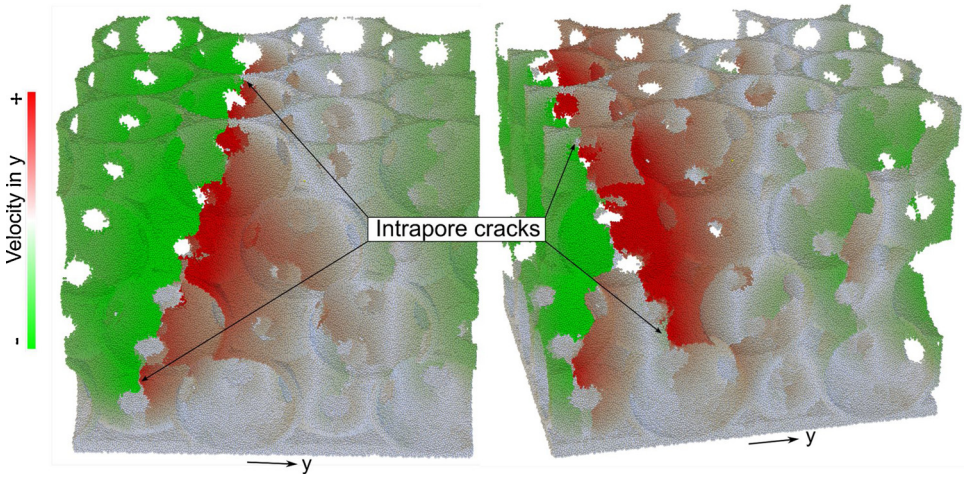

Fig. 10. Material motion for two ideally ordered FCC structures. Formation of the intrapore cracks across several macropores can be seen from the heterogeneity of particle dynamics.

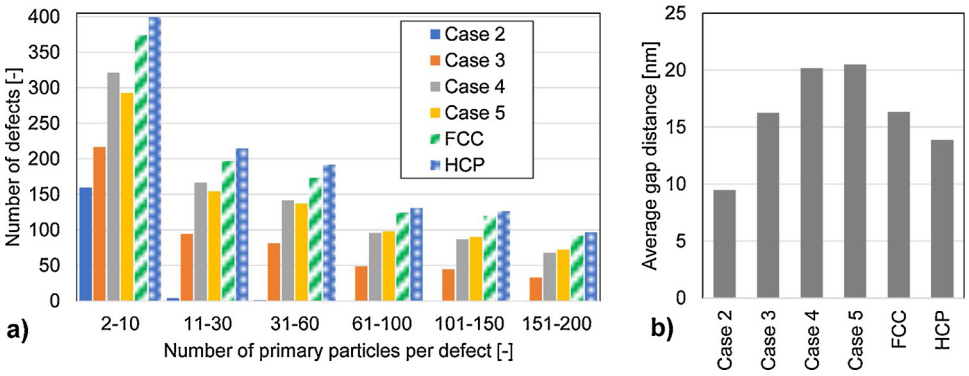

Fig. 11. Comparison of defects formation for different case studies: a) total number of defects consisting of a different number of primary particles (proportional to the formation of a new surface); b) average gap distance calculated with Eq. (5).

and implemented into the simulation framework MUSEN. In order to reach the necessary spatial resolution, the porous structures of reflective thermal barrier coatings (rTBCs) have been represented with approximately 1.2 million primary particles. Usage of the GPU parallelization combined with the periodic boundary conditions has allowed to perform calculations in a reasonable time.

The influence of different packing structures of polymeric template particles on the stability of inverse opal rTBCs was simulated and compared with experimental results. It was observed that defects start preferentially at the former connection points between template particles and propagate leading to the formation of interpore cracks with lengths ranging from 50 to 700 nm. On the later stages, intrapore cracks with lengths exceeding 700 nm are formed. The obtained numerical results are in very good agreement with the experimental data, where similar crack patterns have been observed in SEM images.

Results have shown that, on the one hand, increased packing densities had a positive effect, which results in smaller overall deformation of rTBC. However, on the other hand, higher densities can have a negative effect leading to the formation of a larger number of defects. This is a very interesting finding, as the thermal stability of such photonic structures depends both on the formation of defects and on the overall deformation. While the first could result in cracks propagating from inside the structure, which reduce the photonic capability, the second can lead to delamination of the entire film in case the stresses generated by this deformation are not entirely relaxed and exceed the interfacial strength. Overall, photonic glasses are better suited for reflective thermal barrier coatings in terms of reflectance capability, and our results point out less defect formation, but indicate that special attention should be given to the interfacial strength between photonic structure and substrate, as these structures deform more when exposed to higher temperatures.

Declaration of Competing Interest

The authors declare that they have no known competing financial interests or personal relationships that could have appeared to influence the work reported in this paper

Acknowledgments

Funded by the Deutsche Forschungsgemeinschaft (DFG, German Research Foundation) – Project number 192346071 – SFB 986 (projects A3 and C5).

References

[1] H.S. Lee, R. Kubrin, R. Zierold, A.Y. Petrov, K. Nielsch, G.A. Schneider, M. Eich, Thermal radiation transmission and reflection properties of ceramic 3D photonic crystals, J. Opt. Soc. Am. B 29 (2012) 450, https://doi.org/10.1364/JOSAB.29.000450.

[2] V. Shklover, L. Braginsky, G. Witz, M. Mishrikey, C. Hafner, High-temperature photonic structures. thermal barrier coatings, infrared sources and other applications, J. Comput. Theor. Nanosci. 5 (2008) 862–893, https://doi.org/10.1166/jctn.2008.2532.

[3] Y.X. Yeng, M. Ghebrebrhan, P. Bermel, W.R. Chan, J.D. Joannopoulos, M. Soljacic, I. Celanovic, Enabling high-temperature nanophotonics for energy applications, Proc. Natl. Acad. Sci. U. S. A. 109 (2012) 2280–2285, https://doi.org/10.1073/pnas.1120149109.

[4] N. Vogel, M. Retsch, C.-A. Fustin, A. Del Campo, U. Jonas, Advances in colloidal

assembly: the design of structure and hierarchy in two and three dimensions, Chem. Rev. 115 (2015) 6265–6311, https://doi.org/10.1021/cr400081d.
[5] B. Hatton, L. Mishchenko, S. Davis, K.H. Sandhage, J. Aizenberg, Assembly of large-area, highly ordered, crack-free inverse opal films, Proc. Natl. Acad. Sci. U. S. A. 107 (2010) 10354–10359, https://doi.org/10.1073/pnas.1000954107.
[6] J.J. do Rosário, E.T. Lilleodden, M. Waleczek, R. Kubrin, A.Y. Petrov, P.N. Dyachenko, J.E.C. Sabisch, K. Nielsch, N. Huber, M. Eich, G.A. Schneider, Self-assembled ultra high strength, ultra stiff mechanical metamaterials based on inverse opals, Adv. Eng. Mater. 17 (2015) 1420–1424, https://doi.org/10.1002/adem.201500118.
[7] R. Kubrin, J.J. do Rosario, H.S. Lee, S. Mohanty, R.P. Subrahmanyam, I. Smirnova, A. Petrov, A.Y. Petrov, M. Eich, G.A. Schneider, Vertical convective coassembly of refractory YSZ inverse opals from crystalline nanoparticles, ACS Appl. Mater. Interfaces 5 (2013) 13146–13152, https://doi.org/10.1021/am404180y.
[8] S. Sokolov, D. Bell, A. Stein, Preparation and characterization of macroporous α-Alumina, J. Am. Ceram. Soc. 86 (2003) 1481–1486, https://doi.org/10.1111/j.1151-2916.2003.tb03500.x.
[9] H.M. Yates, M.E. Pemble, A. Blanco, H. Míguez, C. López, F. Meseguer, Growth of tin oxide in opal, Chem. Vap. Deposit. 6 (2000) 283–285, https://doi.org/10.1002/1521-3862(200011)6:6<283::AID-CVDE283>3.0.CO;2-S.
[10] R.M. Pasquarelli, H.S. Lee, R. Kubrin, R. Zierold, A.Y. Petrov, K. Nielsch, G.A. Schneider, M. Eich, R. Janssen, Enhanced structural and phase stability of titania inverse opals, J. Eur. Ceram. Soc. 35 (2015) 3103–3109, https://doi.org/10.1016/j.jeurceramsoc.2015.04.041.
[11] M. Knez, K. Nielsch, L. Niinistö, Synthesis and surface engineering of complex nanostructures by atomic layer deposition, Adv. Mater 19 (2007) 3425–3438, https://doi.org/10.1002/adma.200700079.
[12] F. Tang, H. Fudouzi, Y. Sakka, Fabrication of macroporous alumina with tailored porosity, J. Am. Ceram. Soc. 86 (2003) 2050–2054, https://doi.org/10.1111/j.1151-2916.2003.tb03607.x.
[13] K.P. Furlan, E. Larsson, A. Diaz, M. Holler, T. Krekeler, M. Ritter, A.Y. Petrov, M. Eich, R. Blick, G.A. Schneider, I. Greving, R. Zierold, R. Janßen, Photonic materials for high-temperature applications: synthesis and characterization by X-ray ptychographic tomography, Appl. Mater. Today 13 (2018) 359–369, https://doi.org/10.1016/j.apmt.2018.10.002.
[14] Y. Jia, C. Duran, Y. Hotta, K. Sato, K. Watari, Macroporous ZrO_2 ceramics prepared from colloidally stable nanoparticles building blocks and organic templates, J. Colloid Interface Sci. 291 (2005) 292–295, https://doi.org/10.1016/j.jcis.2005.04.083.
[15] J.J. do Rosário, P.N. Dyachenko, R. Kubrin, R.M. Pasquarelli, A.Y. Petrov, M. Eich, G.A. Schneider, Facile deposition of YSZ-Inverse photonic glass films, ACS Appl. Mater. Interfaces 6 (2014) 12335–12345, https://doi.org/10.1021/am502110p.
[16] S.G. Rudisill, Z. Wang, A. Stein, Maintaining the structure of templated porous materials for reactive and high-temperature applications, Langmuir 28 (2012) 7310–7324, https://doi.org/10.1021/la300517g.
[17] J.J. do Rosário, Y. Häntsch, R.M. Pasquarelli, P.N. Dyachenko, E. Vriend, A.Y. Petrov, K.P. Furlan, M. Eich, G.A. Schneider, Advancing the fabrication of YSZ-inverse photonic glasses for broadband omnidirectional reflector films, J. Eur. Ceram. Soc. 39 (2019) 3353–3363, https://doi.org/10.1016/j.jeurceramsoc.2019.04.028.
[18] M. Ogurreck, J.J. do Rosario, E.W. Leib, D. Laipple, I. Greving, F. Marschall, A. Last, G.A. Schneider, T. Vossmeyer, H. Weller, F. Beckmann, M. Müller, Determination of the packing fraction in photonic glass using synchrotron radiation nanotomography, J. Synchrotron Radiat. 23 (2016) 1440–1446, https://doi.org/10.1107/S1600577516012960.
[19] C. Ying-Chieh, J.B. Geddes, L. Yin, P. Wiltzius, P.V. Braun, X-ray computed tomography of holographically fabricated three-dimensional photonic crystals, Adv. Mater. 24 (2012) 2863–2868, https://doi.org/10.1002/adma.201200411.
[20] S. Flenner, E. Larsson, K.P. Furlan, D. Laipple, M. Storm, F. Wilde, R. Blick, G.A. Schneider, R. Zierold, R. Janssen, et al., Nanotomography of inverse photonic crystals using zernike phase contrast, Microsc. Microanal. 24 (2018) 148–149, https://doi.org/10.1017/S1431927618013120.
[21] M. Dosta, M. Weber, V. Schmidt, S. Antonyuk, DEM analysis of breakage behavior of bicomponent agglomerates, in: S. Antonyuk (Ed.), Particles in Contact, Springer, 2019, , https://doi.org/10.1007/978-3-030-15899-6_6.
[22] B. Heinrich, A. Wonisch, T. Kraft, M. Moseler, H. Riedel, Simulations of the influence of rearrangement during sintering, Acta Mater. 55 (2007) 753–762, https://doi.org/10.1016/j.actamat.2006.09.005.
[23] C.L. Martin, R.K. Bordia, The effect of a substrate on the sintering of constrained films, Acta Mater. 57 (2009) 549–558, https://doi.org/10.1016/j.actamat.2008.09.041.
[24] R. Besler, M. Rossetti, M. Dosta, S. Heinrich, R. Janssen, Simulation of high temperature behavior of periodic macro porous alumina, J. Am. Ceram. Soc. 26 (2015) 1021–1030, https://doi.org/10.1111/jace.13684.
[25] T. Rasp, C. Jamin, O. Guillon, T. Kraft, Cracking and shape deformation of cylindrical cavities during constrained sintering, J. Eur. Ceram. Soc. 37 (2017) 2907–2917, https://doi.org/10.1016/j.jeurceramsoc.2017.03.013.
[26] A. Lichtner, D. Roussel, D. Röhrens, D. Jauffres, J. Villanova, C.L. Martin, R.K. Bordia, Anisotropic sintering behavior of freeze-cast ceramics by optical dilatometry and discrete-element simulations, Acta Mater. 155 (2018) 344–349, https://doi.org/10.1016/j.actamat.2018.06.001.
[27] S. Nosewicz, J. Rojek, K. Wawrzyk, P. Kowalczyk, G. Maciejewski, M. Maździarz, Multiscale modeling of pressure-assisted sintering, Comput. Mater. Sci. 156 (2019) 385–395, https://doi.org/10.1016/j.commatsci.2018.10.001.
[28] R. Besler, M.R. da Silva, M. Dosta, S. Heinrich, R. Janssen, Discrete element simulation of metal ceramic composite materials with varying metal content, J. Eur. Ceram. Soc. 36 (2016) 2245–2253, https://doi.org/10.1016/j.jeurceramsoc.2015.12.051.
[29] V. Iacobellis, A. Radhi, K. Behdinan, Discrete element model for ZrB_2-SiC ceramic composite sintering, Compos. Struct. 229 (2019) 111373, https://doi.org/10.1016/j.compstruct.2019.111373.
[30] D. Jauffrés, C.L. Martin, A. Lichtner, R.K. Bordia, Simulation of the toughness of partially sintered ceramics with realistic microstructures, Acta Mater. 60 (2012) 4685–4694, https://doi.org/10.1016/j.actamat.2012.05.024.
[31] Y. Xie, R. Xing, Q. Li, L. Xu, H. Song, Three-dimensional ordered ZnO–CuO inverse opals toward low concentration acetone detection for exhaled breath sensing, Sens. Actuators B Chem. 211 (2015) 255–262, https://doi.org/10.1016/j.snb.2015.01.086.
[32] K.P. Furlan, T. Krekeler, M. Ritter, R. Blick, G.A. Schneider, K. Nielsch, R. Zierold, R. Janßen, Low-temperature mullite formation in ternary oxide coatings deposited by ald for high-temperature applications, Adv. Mater. Interfaces 4 (2017), https://doi.org/10.1002/admi.201700912.
[33] K.P. Furlan, R.M. Pasquarelli, T. Krekeler, M. Ritter, R. Zierold, K. Nielsch, G.A. Schneider, R. Janssen, Highly porous α-Al_2O_3 ceramics obtained by sintering atomic layer deposited inverse opals, Ceram. Int. 43 (2017) 11260–11264, https://doi.org/10.1016/j.ceramint.2017.05.176.
[34] A. Spettl, S. Bachstein, M. Dosta, M. Goslinska, S. Heinrich, V. Schmidt, Bonded-particle extraction and stochastic modeling of internal agglomerate structures, Adv. Powder Technol. 27 (2016) 1761–1774, https://doi.org/10.1016/j.apt.2016.06.007.
[35] H.G. Campos, K.P. Furlan, D.E. Garcia, R. Blick, R. Zierold, M. Eich, D. Hotza, R. Janssen, Effects of processing parameters on 3D structural ordering and optical properties of inverse opal photonic crystals produced by atomic layer deposition, Int. J. Ceram. Eng. Sci. 1 (2019) 68–76, https://doi.org/10.1002/ces2.10015.
[36] S. Torquato, T.M. Truskett, P.G. Debenedetti, Is random close packing of spheres well defined? Phys. Rev. Lett. 84 (2000) 2064–2067, https://doi.org/10.1103/PhysRevLett.84.2064.
[37] F. Parhami, R. McMeeking, A network model for initial stage sintering, Mech. Mater. 2 (1998) 111–124, https://doi.org/10.1016/S0167-6636(97)00034-3.
[38] C. O'Sullivan, J.D. Bray, Selecting a suitable time step for discrete element simulations that use the central difference time integration scheme, Eng. Comput. 21 (2003) 278–303, https://doi.org/10.1108/02644400410519794.
[39] S. Nosewicz, J. Rojek, K. Pietrzak, M. Chmielewski, Viscoelastic discrete element model of powder sintering, Powder Technol. 246 (2013) 157–168, https://doi.org/10.1016/j.powtec.2013.05.020.
[40] S. Martin, M. Guessasma, J. Léchelle, J. Fortin, K. Saleh, F. Adenot, Simulation of sintering using a non smooth discrete element method. Application to the study of rearrangement, Computat. Mater. Sci. 84 (2014) 31–39, https://doi.org/10.1016/j.commatsci.2013.11.050.
[41] A. Wonisch, O. Guillon, T. Kraft, M. Moseler, H. Riedel, J. Rödel, Stress-induced anisotropy of sintering alumina: discrete element modelling and experiments, Acta Mater. 55 (2007) 5187–5199, https://doi.org/10.1016/j.actamat.2007.05.038.
[42] A. Kinloch, Adhesion and Adhesives, Springer, Netherlands, 1987.
[43] O.A. Ruano, J. Wadsworth, O.D. Sherby, Deformation of fine-grained alumina by grain boundary sliding accommodated by slip, Acta Mater. 51 (2003) 3617–3634, https://doi.org/10.1016/S1359-6454(03)00180-0.